

Shock formation and nonlinear saturation effects in the ultrasound field of a diagnostic curvilinear probe

Maria M. Karzova,^{a)} Petr V. Yuldashev, Oleg A. Sapozhnikov,^{b)} and Vera A. Khokhlova^{b)}
Physics Faculty, Moscow State University, Moscow 119991, Russia

Bryan W. Cunitz, Wayne Kreider, and Michael R. Bailey
Center for Industrial and Medical Ultrasound, Applied Physics Laboratory, University of Washington, 1013 NE 40th Street, Seattle, Washington 98105, USA

(Received 14 December 2016; revised 13 March 2017; accepted 14 March 2017; published online 4 April 2017)

Newer imaging and therapeutic ultrasound technologies may benefit from *in situ* pressure levels higher than conventional diagnostic ultrasound. One example is the recently developed use of ultrasonic radiation force to move kidney stones and residual fragments out of the urinary collecting system. A commercial diagnostic 2.3 MHz C5-2 array probe has been used to deliver the acoustic pushing pulses. The probe is a curvilinear array comprising 128 elements equally spaced along a convex cylindrical surface. The effectiveness of the treatment can be increased by using higher transducer output to provide a stronger pushing force; however nonlinear acoustic saturation can be a limiting factor. In this work nonlinear propagation effects were analyzed for the C5-2 transducer using a combined measurement and modeling approach. Simulations were based on the three-dimensional Westervelt equation with the boundary condition set to match low power measurements of the acoustic pressure field. Nonlinear focal waveforms simulated for different numbers of operating elements of the array at several output power levels were compared to fiber-optic hydrophone measurements and were found to be in good agreement. It was shown that saturation effects do limit the acoustic pressure in the focal region of a diagnostic imaging probe.

© 2017 Acoustical Society of America. [<http://dx.doi.org/10.1121/1.4979261>]

[JFL]

Pages: 2327–2337

I. INTRODUCTION

Among new imaging and therapeutic ultrasound techniques there are applications that may safely benefit from higher *in situ* pressure levels compared to conventional diagnostic values.¹ These applications generally use acoustic radiation force to induce displacements of tissue or calculi *in vivo*. Localized displacements of tissue are used in shear wave elasticity imaging² to determine elastic moduli that are associated with pathological tissues. Displacements of solid concretions are used in the recently developed method of kidney stone propulsion.^{3–5}

Kidney stone disease (nephrolithiasis) is a common urological condition that afflicts about 10% of the population during their lifetimes.⁶ All stone surgeries can leave residual fragments that are expected to pass naturally but may not in a substantial number of cases. Shock wave lithotripsy (SWL) is the medical procedure that is widely used for extracorporeal removal of kidney stones. It utilizes high-energy focused shock pulses to break stones into small fragments that can pass from the body naturally.⁷ However, persistence of residual stone fragments in the lower pole of the kidney is a common problem confronted by urologists and documented in 21%–59% of patients who underwent SWL.⁸ Residual stones

remain after ureteroscopy in the lower pole about 35% of the time.⁹

Ultrasonic propulsion is a new technology to reposition kidney stones noninvasively—either to aid passage or to relieve obstruction and pain.^{3,4} It can be used to remove small kidney stones by pushing them toward the ureter, or as an effective method to facilitate passage of stone fragments after surgery. The first clinical prototype of this technology includes a diagnostic ultrasound probe to create a real-time B-mode image and to generate a pulse for moving the kidney stone with acoustic radiation force (see Fig. 1).¹⁰ Preliminary investigative clinical results obtained using this prototype have been successful; 4 of 6 post surgery subjects collectively passed over 30 fragments following ultrasonic propulsion.¹¹ Although these trials were conducted at essentially diagnostic levels, many of the issues discussed in the current paper were observed while developing and testing the system; potentially, the efficacy of the procedure may be increased by using higher *in situ* pressure to generate greater radiation force. For example, stones as large as 10 mm were moved in the clinical trial, but perhaps the procedure could benefit from higher pressure and radiation force such as moving larger stones from an obstructing location or from the lower pole before surgery.

In calibration measurements of the field generated by the ultrasonic propulsion probe in water, it was observed that at some output level an increase in power did not result in an increase in the focal pressure. The hypothesis was that shock formation and nonlinear acoustic saturation in the ultrasound

^{a)}Electronic mail: masha@acs366.phys.msu.ru

^{b)}Also at: Center for Industrial and Medical Ultrasound, Applied Physics Laboratory, University of Washington, 1013 NE 40th Street, Seattle, WA 98105, USA.

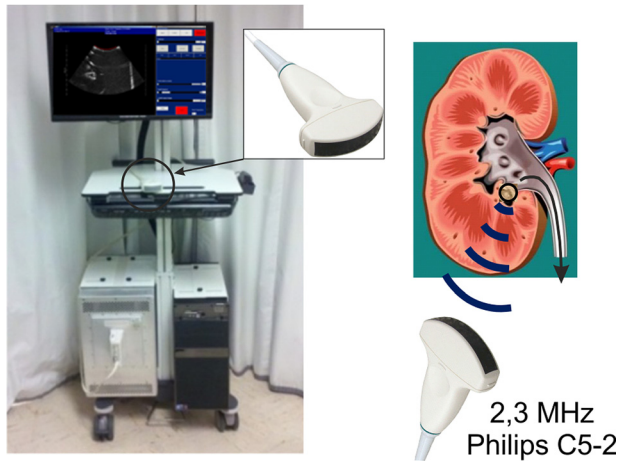


FIG. 1. (Color online) Ultrasonic propulsion system (on left) and illustration of the new method to push kidney stones (on right).

beam was the limiting factor.^{12,13} The goal of this paper was to test this hypothesis and to evaluate the degree of these strong nonlinear effects at operational power outputs.

Previously, nonlinear propagation of diagnostic ultrasound pulses was investigated to study the spatial distribution of fundamental and second harmonic frequencies for application to tissue harmonic imaging (THI).^{14–16} However, in THI, weakly nonlinear regimes are used, while in ultrasonic propulsion research we found that an unmodified convex imaging probe driven at conventional diagnostic voltages could be focused to generate shocks in the imaging field of view. The presence of a shock front changes the pressure field structure and complicates the field characterization of the probe. Such strong nonlinear effects in the fields of diagnostic transducers have not been studied in detail. In addition, most previous studies were performed for flat rectangular-shaped clinical scanners.^{14–16} In this paper, the more complicated case of a curvilinear array is considered.

Accurate characterization of nonlinear ultrasound fields generated by various high intensity focused medical devices has recently been performed using a combined measurement and modeling approach.^{17–20} This approach uses numerical modeling for detailed analysis of spatial and temporal structures of nonlinear fields while measurements are used to set a boundary condition and to validate modeling results. Both axially symmetric single element sources^{17–19} and multi-element arrays²⁰ with approximate axial symmetry have been characterized. Here, the combined measurement and modeling approach is first implemented for nonlinear acoustic fields generated by a diagnostic curvilinear array. The modeling part is based on the three-dimensional (3D) Westervelt equation which accounts for the combined effects of nonlinearity, diffraction, and thermoviscous absorption. The boundary condition in simulations was set to match axial beam scans of the acoustic pressure field acquired at low power in water. Nonlinear focal waveforms were measured by fiber-optic hydrophone for various output power levels of the probe to validate results of the simulations.

The content of the paper is organized as described here. The experimental setup is described first (Sec. II A). Then,

the numerical model and details of the combined measurement and modeling approach for field characterization are presented (Sec. II B), followed by the procedure of setting a boundary condition to the model (Sec. II C). Next, linear simulation results are reported and compared with low power measurements performed for a variable number of operating elements (Sec. III A). Finally, nonlinear modeling data validated against measurements collected at the focus over a wide range of clinically relevant output power levels are presented and discussed (Secs. III B and III C). The spatial structures of the peak positive pressure, peak negative pressure, and intensity are analyzed including the ultrasound field structure at the highest operational level of the probe. The results are summarized in Sec. IV.

II. MATERIALS AND METHODS

A. Experimental arrangement and transducer array details

The experimental setup used to measure pressure fields generated by an abdominal imaging probe (Philips C5-2, Bothell, WA) is depicted in Fig. 2. The imaging probe was driven by a V-1 Verasonics ultrasound engine with extended transmit burst capabilities (Verasonics, Kirkland, WA); the Verasonics was controlled through a personal computer (HP Z820, Palo Alto, CA) using custom MATLAB programs (Mathworks, Natick, MA). The probe axis was directed vertically in a large water tank, facing downwards. Water was degassed to about 10% dissolved oxygen. The axes of the probe were aligned to those of a 3-axis positioner (Velmex, Bloomfield, NY). A hydrophone was mounted to the positioner by a custom L-shaped fixture so that the fiber was parallel to the ultrasound beam axis.

The transmit signals were 75 cycles at 2.3 MHz frequency with a pulse repetition rate of 20 Hz. A trigger signal

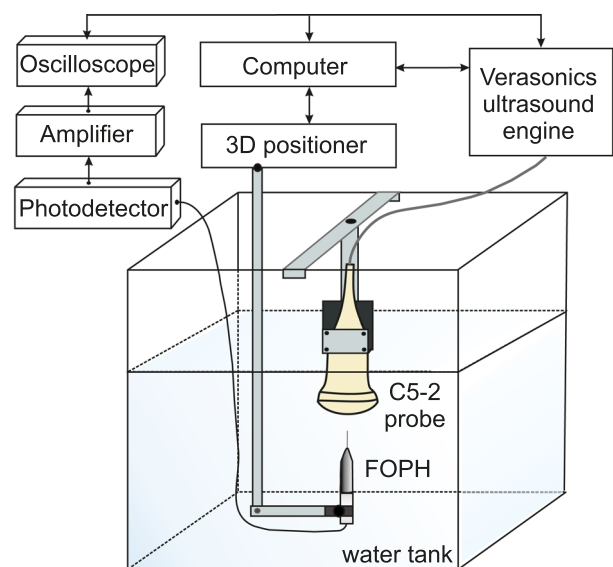


FIG. 2. (Color online) Diagram of the experimental arrangement for acoustic field measurements in water. A FOPH was used for high-amplitude measurements while low-amplitude measurements were performed using a capsule hydrophone.

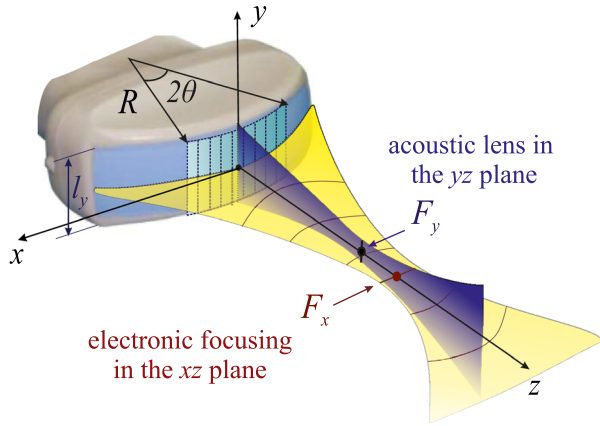


FIG. 3. (Color online) Geometry of the C5-2 diagnostic curvilinear probe.

was generated by the Verasonics at the beginning of the transmission to synchronize oscilloscope acquisition.

The C5-2 curvilinear array probe comprises 128 single elements and has a cylindrical shape with radius of curvature R , aperture angle 2θ , height l_y , and two focal lengths, F_x and F_y (see Fig. 3). Steering of the focus F_x in the scanning plane xz is performed electronically by changing the voltage phase over the probe elements. A cylindrical acoustic lens focuses the field at a constant depth F_y to reduce the divergence of the beam in the elevation plane yz . Field measurements were performed with 16, 32, 40, 64, and 128 active elements; the centermost elements were used for each configuration.

Nominal dimensions of the probe were measured by a ruler: radius of curvature $R \approx 38$ mm, aperture angle $2\theta \approx 40^\circ$, and height $l_y \approx 12$ mm (see Fig. 3). While these values are not exact, they provided an initial approximation for identifying the parameters of an equivalent source in numerical modeling. The product specification sheet from the manufacturer provided nominal values of the width of each element (0.37 mm) and the gap between them (0.05 mm). In experiments, delays to each of the elements of the probe were programmed by a time of flight calculated using the values of the speed of sound in water as 1486 m/s and a focal position of $z = F_x = 50$ mm along the axis of the probe.

The hydrophone measurements included two steps. First, low-amplitude measurements of pressure waveforms were performed using a capsule hydrophone in conjunction with a preamplifier (HGL-0085 and AH-2010, Onda, Sunnyvale, CA). The sensitive surface of the hydrophone was a polyvinylidene difluoride membrane of 85 μm diameter; the calibrated frequency range spans from 1 to 20 MHz. Pressure amplitude distributions were measured along the beam axis z and in two perpendicular directions x and y in the focal plane at $z = 50$ mm. These measurements were carried out at the lowest possible voltage (2 V) applied to the probe and were used for setting a boundary condition to the numerical model. The step size along the z axis was 0.5 mm while transverse scans were done with steps of 0.1 and 0.05 mm along the x axis and y axis, respectively.

The second step of measurements was carried out by increasing the voltage applied to the array across the range from 5 to 90 V. Nonlinear pressure fields were measured

using a fiber optic hydrophone (FOPH 2000, RP Acoustics, Leutenbach, Germany) with a fiber tip of 100 μm in diameter, nominal sensitivity of 2 mV/MPa, bandwidth of 100 MHz, and a noise floor level of about 2 MPa.^{18,21} The location of the maximum of the peak positive pressure on the beam axis was determined using a transmit sequence with 128 elements at 50 V. The FOPH was translated through the region close to the focus first along the axis and then in the transverse directions with a step size of 25 μm to identify the location of the pressure maximum. At this location that corresponded to $z = 50$ mm, all the waveforms were collected at increasing voltage levels for different numbers of operating elements. Averages of the pressure waveform (128) were used at each acquisition point with the FOPH bandwidth set at 100 MHz and a sampling rate of 320 MHz. The averaged waveform then was deconvolved using the time-domain impulse response supplied by the manufacturer for the FOPH.^{18,21,22} Mean and standard deviation values for peak positive and negative pressure were taken between the 50th and 74th cycles so that a steady state level of peak pressure was reached in the waveform. These measurements were compared with nonlinear modeling results.

B. Numerical model

A 3D numerical model based on the Westervelt equation²³ was used to simulate the nonlinear acoustic field generated in water by the diagnostic probe at different output levels and for different numbers of operating elements. The model is described in detail in the earlier studies in Refs. 20 and 24. Here we briefly summarize the main concepts of the numerical algorithm and its implementation.

The Westervelt equation written in a retarded time coordinate is given as

$$\frac{\partial^2 p}{\partial \tau \partial z} = \frac{c_0}{2} \Delta p + \frac{\beta}{2\rho_0 c_0^3} \frac{\partial^2 p^2}{\partial \tau^2} + \frac{\delta}{2c_0^3} \frac{\partial^3 p}{\partial \tau^3}. \quad (1)$$

Here p is pressure, $\tau = t - z/c_0$ is the retarded time, and $\Delta p = \partial^2 p / \partial z^2 + \partial^2 p / \partial y^2 + \partial^2 p / \partial x^2$. Parameters of the propagation medium, c_0 , ρ_0 , β , and δ are the ambient sound speed, the density, the coefficient of nonlinearity, and the thermoviscous absorption, respectively. The values of the parameters were chosen to represent the experimental measurement conditions in water at room temperature: $\rho_0 = 998$ kg/m³, $c_0 = 1486$ m/s, $\beta = 3.5$, $\delta = 4.33 \times 10^6$ m²/s. The Westervelt Eq. (1) accounts for the combined effects of nonlinearity, diffraction, and thermoviscous absorption. This is a full-diffraction nonlinear model that does not require a narrow focusing angle of the field.

Simulations of Eq. (1) were performed using the method of fractional steps with an operator splitting procedure of second-order accuracy both in time and space.¹⁸ The diffraction operator was calculated in the frequency domain for each harmonic component using the angular spectrum method. The absorption was calculated also in the frequency domain using an exact solution for each harmonic. The nonlinear operator was calculated in the frequency domain using the fourth-order Runge-Kutta method at small distances

from the probe and using a conservative time-domain Godunov-type scheme at greater distances. The switch to the Godunov-type scheme was made at a distance z where the amplitude of the tenth harmonic exceeded 1% of the amplitude of the fundamental frequency f . Parameters of the numerical scheme were: longitudinal step $dz = 0.075$ mm, transverse steps $dx = dy = 0.02$ mm. The maximum number of harmonics was 750. Following a recently proposed method, the formation of a fully developed shock in the simulated focal waveform corresponded to the situation when the bottom of the shock coincided with the zero pressure level.²⁵

C. Setting the boundary condition using low-amplitude beam scans

To ensure accurate simulation of experimental conditions, it was necessary to set an appropriate boundary condition to the Westervelt equation [Eq. (1)] at the initial plane ($x, y, z = 0$). A simplified source model that corresponds to the geometry of the C5-2 array probe and produces the same (“equivalent”) acoustic field was developed. Toward this end, continuous wave conditions at frequency $f = 2.3$ MHz were simulated by setting a uniform amplitude of normal velocity over the cylindrical surface of the equivalent source. The phase was changed continuously over this surface in the y and θ directions to provide focusing, thereby defining the surface velocity of the transducer as

$$u(R, \theta, y) = \frac{p_0}{\rho_0 c_0} \sin[2\pi f t + k(\Delta x + y^2/2F_y)], \quad (2)$$

with $u(R, \theta, y) = 0$ beyond the vibrating surface. Here, (R, θ, y) is a cylindrical coordinate system with its origin at the center of curvature of the probe, p_0 is the characteristic source pressure amplitude, $k = 2\pi f/c_0$ is the wavenumber, and t is time. Note that $\Delta x = \sqrt{(R \sin \theta)^2 + (R - R \cos \theta + F_x)^2} - F_x$ is the difference between the propagation distances to the focus from the apex of the probe with coordinates $(R, \theta = 0)$ and a selected point on the probe surface at position (R, θ) (see Fig. 3). Changing the number of operating elements was accounted for in the model by changing the aperture angle θ .

The solution in the form of the Rayleigh integral²⁶ was used for calculating the linear acoustic field generated by the probe at a given location \vec{r} ,

$$p(\vec{r}, t) = -i\rho_0 f \int_S \frac{u'(\vec{r}') \exp(ik|\vec{r} - \vec{r}'|)}{|\vec{r} - \vec{r}'|} dS', \quad (3)$$

where $u'(\vec{r}')$ is the complex magnitude of the vibration velocity at the surface S' of the probe.

A boundary condition [Eq. (2)] to the Westervelt equation [Eq. (1)] was set by varying the geometrical parameters of the probe to determine the best fit between measurements at low outputs and linear calculations [Eq. (3)]; distributions of pressure amplitude were considered on the beam axis and in the transverse focal plane.

Since only estimates of the parameters $R, \theta, l_y, p_0, F_x,$ and F_y of the probe were initially known, simulations of the

linear field were carried out in several iterations. First, the axial pressure distribution [Eq. (3)] was calculated for approximate nominal values of $R, \theta,$ and l_y given above in Sec. II A assuming $F_x = F_y = 50$ mm. Then, each of the five parameters $R, \theta, l_y, F_x,$ and F_y was varied individually so that the pressure amplitude distribution normalized by its maximum matched the experimental beam scanning results measured on the beam axis and in the focal plane. Note that each of the parameters determines a specific feature in the distributions and therefore can be determined independently. For example, the parameter l_y has a predominant effect on the pressure distribution in the focal plane along the y axis but has almost no effect on the axial distribution along the z axis. Specifically, l_y determines a position of the side lobes in the distribution along the y axis while the amplitude of these side lobes is determined by the parameter F_y . Parameter F_x was found by fitting the position of maxima in the measured and modeled pressure distributions along the z axis. Angle θ has a strong influence on the position of the side lobes in distributions along both the z and x axes. Finally, radius R determines the width of the focal lobe along the z axis. After finding the best fit values of the parameters $R, \theta, l_y, F_x,$ and F_y for configurations of 16, 32, 40, 64, and 128 active elements, the effective source pressure amplitude p_0 was determined by matching pressure amplitudes at the focus, simulated and measured with a capsule hydrophone at the output voltage $V_0 = 2$ V.

After parameters of the equivalent source were determined at the cylindrical surface, the boundary condition for modeling the 3D nonlinear field of the probe was set on the plane ($x, y, z = 0$) at the apex of the probe. To avoid a singularity of the kernel in the Rayleigh integral [Eq. (3)], the acoustic pressure was calculated first in the plane $z = 2$ mm. Then, the angular spectrum method was used to linearly back-propagate the pressure distribution the apex plane $z = 0$. The resulting distribution was used as a boundary condition to the 3D nonlinear ultrasound field modeling. The pressure amplitude p_0 of the initial harmonic wave was scaled proportionally to the voltage V_0 applied to the probe assuming a linear dependence between voltage and pressure.

III. RESULTS

In this section, modeling results are presented to provide detailed information of spatial distributions of peak pressures and intensity in the acoustic field generated by the probe over a wide range of clinically relevant output power levels and for different numbers of operating elements. Modeling results are validated by comparing acoustic waveforms simulated and measured at the focus for a range of output settings which include levels that produced saturation.

A. Validation of the boundary condition in simulations

The best-fit parameters of the equivalent source are listed in Table I. The radius of curvature R of the probe along with the height l_y were found to be the same for all configurations while the focal depth of the acoustic lens F_y was dependent on the number of active elements. This length was shorter when 64 or 128 elements were excited, which may be explained by the curved surface of the transducer,

TABLE I. Parameters of the equivalent source that provided the best fit between linear simulation results and measurements.

Number of elements	16	32	40	64	128
Angle of aperture θ , rad $\times 10^{-2}$	8.421	16.842	21.053	33.684	67.368
Source pressure amplitude p_0 , kPa	56.0	56.0	48.0	45.6	37.6
Focal depth of acoustic lens F_y , mm	85	86	86	70	70
Other parameters	$F_x = 50$ mm, $R = 38$ mm, $l_y = 12.5$ mm				

which makes the distance from the focal point to the side elements larger than that to the central elements. For the same voltage applied to the probe elements, the source pressure amplitude p_0 was greater for smaller numbers of elements due to less directivity and a shorter path in the absorptive lens to the focus from the central elements.

Linear simulation results for acoustic pressure amplitude in comparison with measurements are presented in Fig. 4 both along the z axis (left column) and in the focal plane along the x and y axes (two right columns). The comparison shows that simulated and measured pressures agree well; therefore the equivalent source model does provide a reasonable representation of the acoustic field generated by the probe.

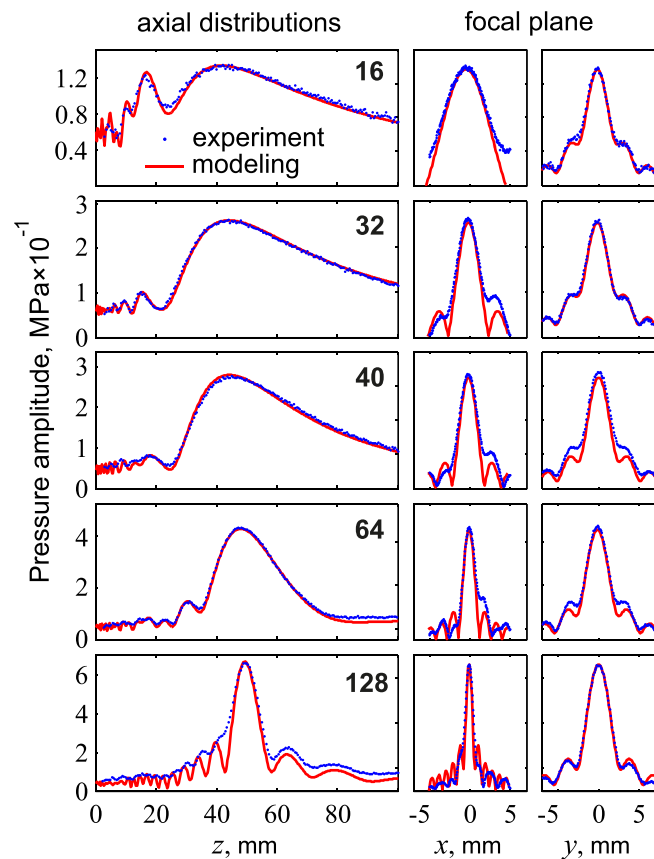


FIG. 4. (Color online) Comparison of simulated and measured acoustic pressure amplitude distributions at the lowest probe output of 2 V (linear propagation). Axial pressure distributions are depicted in the left column while the two right columns depict distributions in two transverse directions in the focal plane at $z = 50$ mm. Results are presented for 16, 32, 40, 64, and 128 active elements of the probe.

The number of active elements of the C5-2 probe determines the width of the probe in the x direction and significantly influences the structure of the acoustic field. With an increasing number of active elements, the dimensions of the focal region along the x and z axes become smaller. For a set of 16 active elements, the focal region at the -3 dB level of the pressure maximum is $6 \times 4 \times 45$ mm along the x , y , and z axes. For 128 elements the focal region is smaller, only $1 \times 4 \times 10$ mm in size. In addition to better spatial localization, for the same voltage applied to the probe, a fivefold increase in the pressure amplitude at the focus is observed with an increase from 16 to 128 elements.

Shown in Fig. 5 are two-dimensional (2D) distributions of the pressure amplitude modeled linearly for different numbers of active elements. The upper series of frames shows distributions of pressure amplitude in a plane transverse to the beam axis and located at a distance of 2 mm from the apex of the probe. Regions of the active surface of the probe are clearly visible as bright areas in the distributions; white dashed contours depict the area of the entire array. Note that interference of waves emitted by each single element of the probe individually provides a different nearfield structure depending on the number of excited elements. For the sets of 16, 32, and 40 elements the nearfield has a non-uniform structure typical for the interference pattern observed for plane rectangular sources: minima and maxima alternate periodically with the same amplitudes along the active surface of the source. The cylindrical shape of the surface becomes crucial when 64 or 128 elements are excited. In these cases, waves emitted by the side elements of the probe are aligned almost tangential to the propagation direction leading to constructive interference of the waves irradiated by these elements and therefore to a pressure increase at the beam edges in the x direction. This effect is most clearly noticeable for the set of 128 elements (Fig. 5, upper series), where the pressure amplitude in front of the central part of the active surface of the probe is half of that close to the edges.

Distributions of pressure amplitude in the plane xz of the electronic focus and in the elevation plane yz (middle and bottom rows in Fig. 5, respectively) illustrate more effective focusing with more active elements. The active surface with 16 excited elements is larger in the y -direction than in the x -direction; thus, the beam is focused in the yz plane more effectively than in the xz plane. The set of 32 elements has a square shaped active surface and therefore similar pressure distributions are observed in both the xz and yz planes. The structure of the focal regions becomes very different when at least half of the elements are excited. The fully active array (128 elements) creates a highly focused acoustic beam with a distinct X-shaped structure in the xz plane near the focus. This structure forms because of constructive interference of waves emitted by the side elements that provides high pressure amplitude close to the edge of the beam.

B. Experimental validation of nonlinear modeling

This section presents the results for nonlinear waveforms simulated at the focus for different source outputs and

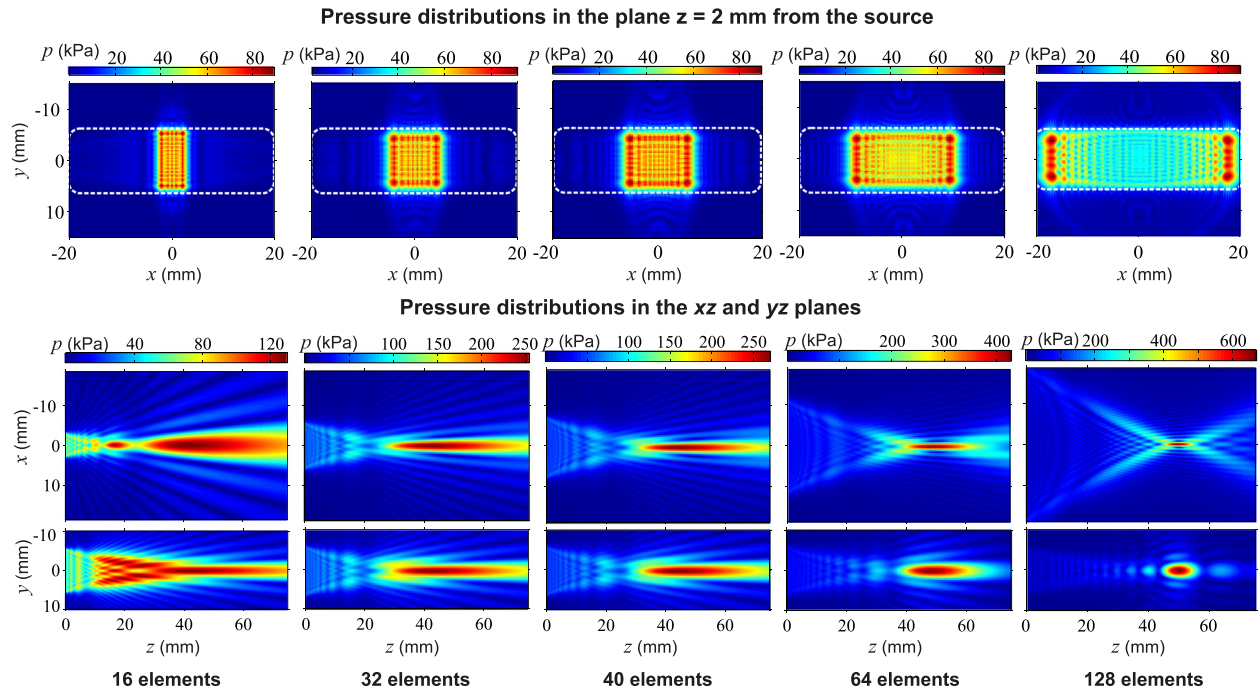


FIG. 5. (Color online) Spatial distributions of the pressure amplitude obtained in the linear simulations for 16, 32, 40, 64, and 128 active elements. White dashed curves in the upper row represent the entire surface of the array.

numbers of operating elements. To validate the accuracy of the modeling, focal waveforms obtained in simulations are compared with direct FOPH measurements at the focus in water for applied voltages ranging from 5 to 90 V.

Examples of the measured and calculated waveforms are shown in Fig. 6 for configurations of 16, 32, 40, 64, and 128 active elements at the applied voltage of 20 V (left column) and 60 V (right column). The waveforms obtained in simulations are in good agreement (within 3%) with the experimental data for all configurations except for some discrepancy in the values of the peak positive pressure for 128 active elements. In this case of using the full aperture of the probe, good agreement was observed for voltages less than 25 V while for higher voltages modeling predicted higher peak positive pressure than was measured (Fig. 6, the case of 60 V for 128 elements). This discrepancy observed is possibly caused by the experimental challenge in accurate positioning of the hydrophone because the beamwidth for the peak positive pressure p_+ in the focal plane becomes even smaller than the diameter of the fiber of the FOPH (100 μm). This problem of measuring a peak pressure in highly focused shock wave fields has been observed previously in the calibration of nonlinear fields produced by a high-power multi-element array of a clinical MR-guided high intensity focused ultrasound (HIFU) therapy system.²⁰

Focal waveforms measured and modeled at the applied voltage of 20 V (left column in Fig. 6) are already strongly asymmetric and contain nearly shocked sections. However, the formation of fully developed shocks occurs at higher voltages: at 22 V for set of 128 elements, then at 23 V for 64 active elements, at 25 V for 40 operating elements, and finally at 30 V for 16 elements. Developed shock fronts with peak positive pressure equal to the shock amplitude therefore

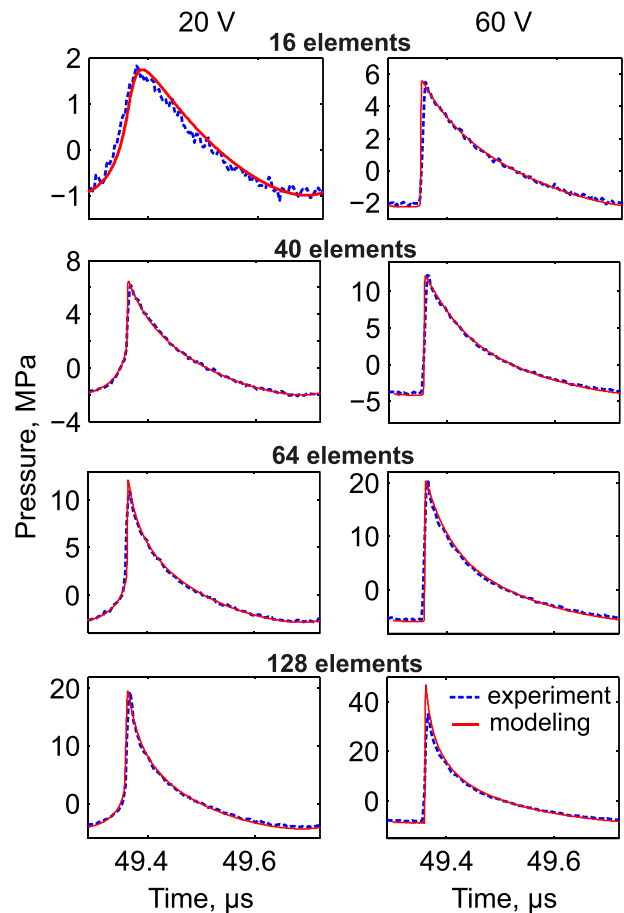


FIG. 6. (Color online) Comparison of the pressure waveforms measured (dashed line) and modeled (solid line) at the distance of $z = 50\text{ mm}$ on the beam axis in water. The left column of frames corresponds to the waveforms measured with an excitation voltage of 20 V and the right column with a voltage of 60 V.

are present at the focus for all configurations of operating elements once the applied voltage reaches about 30 V, which is one-third of the highest operational level (90 V) of the probe used in experiments.

At an output of 60 V (right column in Fig. 6), the waveforms are similar in shape for different sets of operating elements. However, the shock amplitudes differ strongly ranging from 7.7 MPa when operating with 16 elements to 54.9 MPa for 128 elements, with corresponding peak positive pressures of 5.6 and 46.1 MPa and peak negative pressures of -2.1 and -8.8 MPa. For these high power settings, the waveform is close to a symmetric sawtooth wave, and the shock amplitude at the focus is almost equal to the pressure jump between the peak positive and peak negative pressures.

The values of the peak positive p_+ and negative p_- pressures achieved at the focus over the range of all available output levels of the probe are plotted in Fig. 7 for configurations of 16, 32, 40, 64, and 128 active elements. An increase of the applied voltage up to about 20 V leads to a significant increase in the peak positive pressure p_+ , but with further increase, especially above 50 V, the peak positive pressure p_+ begins to saturate due to excess absorption at shock fronts developed on the way to the focus. Previously, the definition of the saturation level was introduced as a 5% threshold of the maximum value of the slope in a saturation curve.²⁷ Following this definition, the peak positive pressure p_+ saturates at 45, 60, 70, 80, and 90 V for the sets of 128, 64, 40, 32, and 16 active elements of the probe.

The limiting values of the peak positive pressure p_+ at the focus predicted in the modeling at the highest operational level of 90 V are ranging from 6.2 MPa (16 elements) to 47.5 MPa (128 elements). For 40 elements the peak positive pressure p_+ is limited to 13.1 MPa in water; the sets of 32 and 64 elements give corresponding values of 10.5 and 21.6 MPa.

The absolute value of the peak negative pressure $|p_-|$ increases monotonically within the whole range of the applied voltages and does not reach saturation. The maximum value of $|p_-|$ at the focus is achieved for the case of

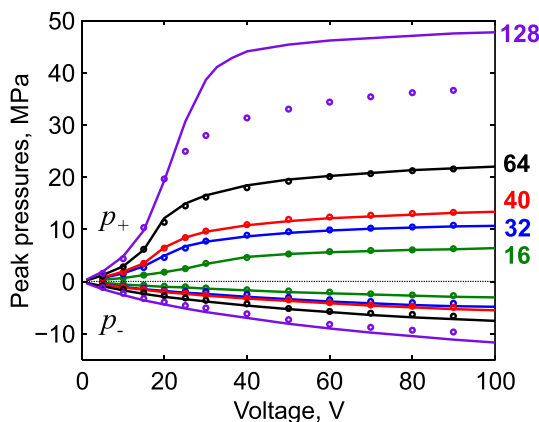


FIG. 7. (Color online) Comparison of the peak positive and peak negative pressures in a focal waveform measured (markers) and modeled (solid curves) at increasing source output in water at $z = 50$ mm for configurations of 16, 32, 40, 64, and 128 active elements.

128 active elements and reaches 10 MPa in water. Excitation of 16, 32, 40, and 64 active elements at the highest operational level of 90 V provide peak negative pressures $|p_-|$ of 2.9, 4.7, 5.2, and 7.2 MPa.

C. Numerical data for nonlinear ultrasound fields at different output voltages

Depicted in Figs. 8 and 9 are the results of nonlinear modeling obtained on a numerical grid one-fifth the size of the FOPH tip and with three times finer time resolution than that provided by the FOPH bandwidth.

Evolution of focal waveforms simulated at increasing applied voltage is shown in Fig. 8 for the configuration of 40 active elements. An initially harmonic waveform at low amplitude (at 5 V) exhibits nonlinear distortion and finally turns into a sawtooth wave containing a shock of increasing amplitude up to 18.3 MPa (profile at 90 V). In the saturation regime, the waveforms do not change significantly with the source output, and the peak pressure values for different applied voltages are only slightly different (profiles at 60 and 90 V).

When nonlinear effects are present, the differences in spatial structure of the acoustic field depend on the element number more strongly than for linearly focused beams. Figure 9 illustrates how the nonlinear acoustic field changes with increasing numbers of active elements.

Initially, when only 16 active elements are excited [Figs. 9(a) and 9(b)], the beam is weakly focused. In this case the strength of the nonlinear effects in the nearfield and in the focal zone of the beam is comparable; therefore, shocks can form in the prefocal lobe leading to excess absorption effects. This results in the sudden shift of the axial maxima of the peak pressures, p_+ and p_- , and intensity I from the main focal to the prefocal diffraction lobe. For the peak positive pressure p_+ this shift of the maximum occurs at the voltage of 80 V while the maximum of the peak negative pressure p_- occurs prefocally above 15 V [Fig. 9(a)]. The intensity I calculated as a sum of intensities of all harmonics becomes higher in the prefocal lobe starting from the voltage of 50 V [Fig. 9(b)].

For the greater number of active elements, the focusing is stronger and the maximum values of the acoustic field

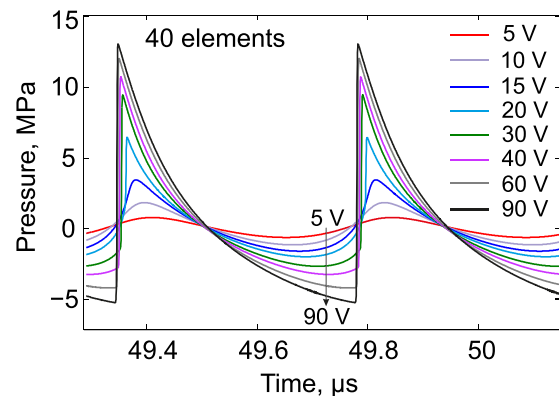


FIG. 8. (Color online) Waveforms at the focus of the probe ($z = 50$ mm) obtained in numerical simulations for 40 active elements.

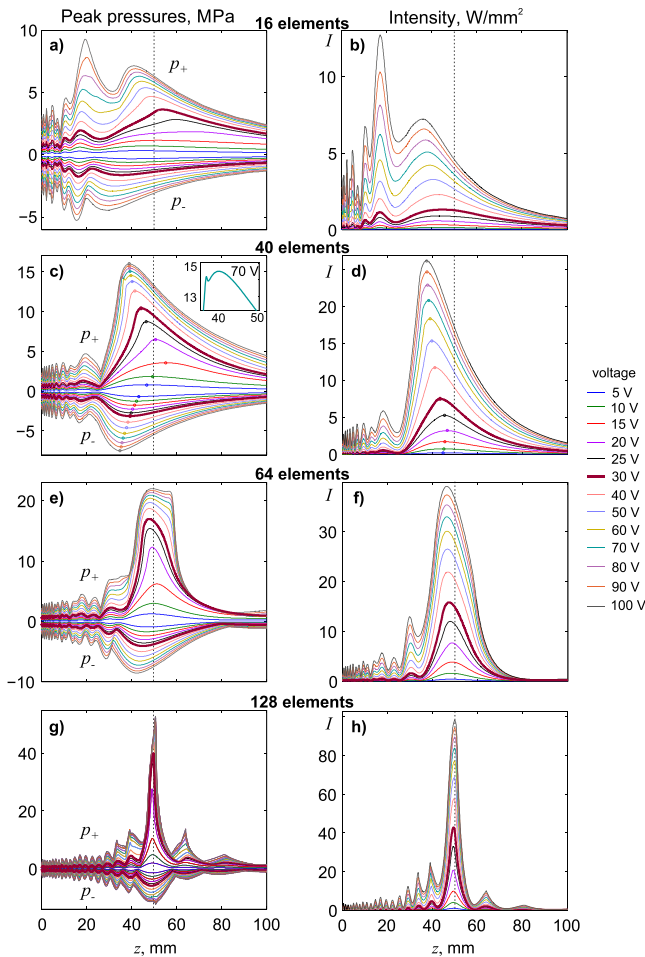


FIG. 9. (Color online) Axial distributions of peak positive and negative pressures (left column) and intensity (right column) obtained in numerical simulations for variable numbers of active elements and voltage levels. The curve in bold corresponds to the applied voltage of 30 V when the developed shock forms at the focus for the 16 element configuration; dashed vertical lines demonstrate the location of the geometrical focus, $z = 50$ mm.

parameters, p^+ , p^- , and I , are achieved in the focal lobe at all applied voltages [Figs. 9(c)–9(h)]. However, displacements of the axial maxima of the peak pressures, p^+ and p^- , and intensity I are observed inside the focal lobe for all sets of elements when changing the voltage [Figs. 9(a)–9(h)]. This effect is the strongest for the set of 40 elements [shown by dots in Figs. 9(c) and 9(d)]. For this configuration, with an increase of the source output, the maximum of p^+ first shifts away from the probe even beyond the depth of electronic focusing, F_x ; then, at voltages greater than 15 V, the maximum shifts toward the probe [Fig. 9(c)]. Such non-monotonic shifts of the spatial maximum of the peak positive pressure p^+ has been observed previously in axially symmetric focused high power ultrasound beams.^{13,24,28,29} An explanation of this phenomenon involves two competing nonlinear effects: nonlinear refraction and nonlinear absorption. At lower outputs, before shocks are formed, a nonlinear refraction effect caused by the higher propagation speed of higher pressures close to the beam axis results in defocusing of the beam and shifts the pressure peak away from the source up to 5 mm from the electronic focus $z = F_x$. At higher outputs, when the shock fronts are developed prefocally, nonlinear absorption at the shocks leads to rapid decay of the beam energy and, as a result, maximal pressure levels are achieved closer to the source. For fully developed shocks, nonlinear absorption is the dominant effect and the pressure maximum shifts toward the source. At the highest output of 100 V used in simulations, the maximum of the peak positive pressure p^+ is shifted 11 mm from the electronic focus $z = F_x$. On the contrary, the maximum of the absolute value of the peak negative pressure $|p^-|$ moves monotonically toward the probe for increasing voltage levels [Fig. 9(c)], with shifts up to 15 mm from the electronic focus $z = F_x$. The intensity maximum I , similar to that of the peak positive pressure p^+ , shifts first away from the probe and then toward the probe [Fig. 9(d)]; however, it is always reached before the electronic focus $z = F_x$ (Fig. 9, right column) for all

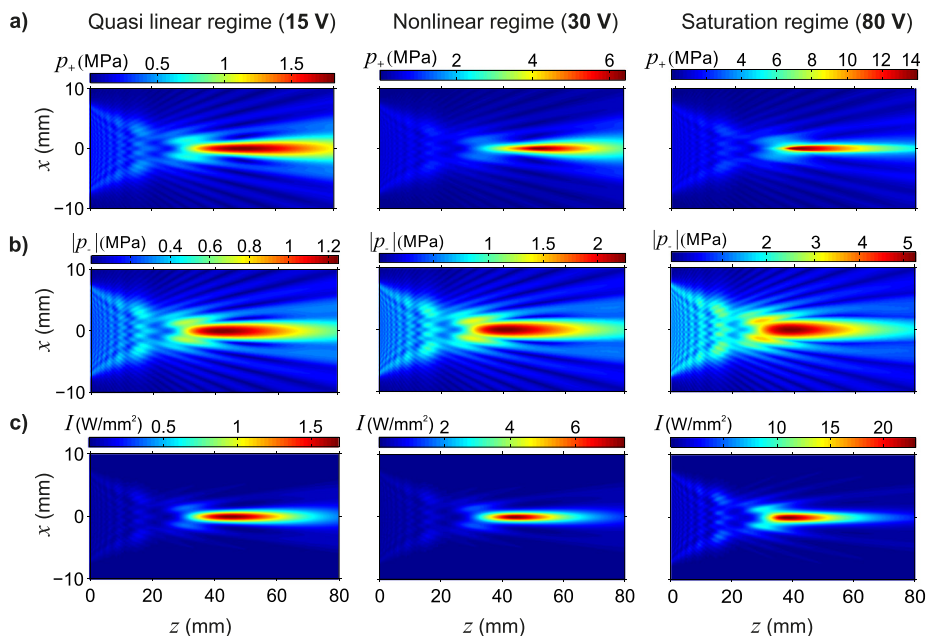


FIG. 10. (Color online) Comparison of 2D spatial distributions of the peak positive pressure (a), peak negative pressure (b), and intensity (c) at applied voltages of 15 V (left column), 30 V (column in the middle), and 80 V (right column) in the case of 40 active elements.

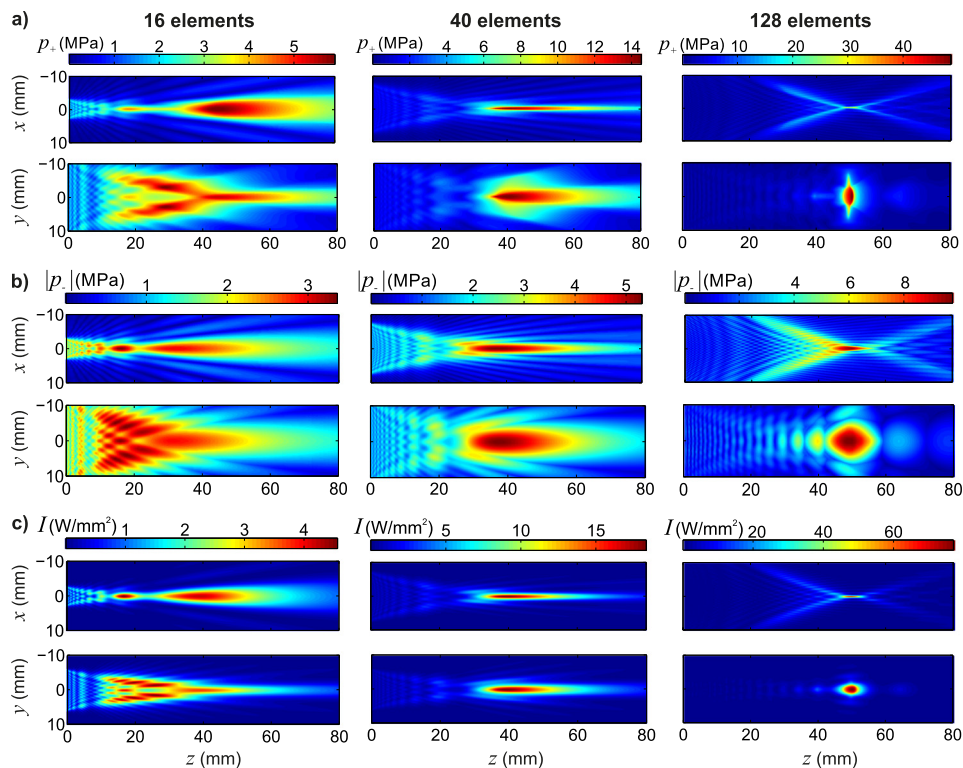


FIG. 11. (Color online) Comparison of 2D spatial distributions of the peak positive pressure (a), peak negative pressure (b), and intensity (c) in a nonlinear regime with an applied voltage of 60 V for configurations of 16, 40, and 128 active elements.

applied voltages. Such displacements of peak pressure and intensity maxima from the electronic focus are smaller for the larger numbers of active elements; for the set of 128 elements this shift does not exceed 1 mm for all parameters, p^+ , p^- , and I .

An interesting nonlinear phenomenon is observed in the saturation regime as illustrated in the inset of Fig. 9(c): the axial distribution of peak positive pressure p^+ contains a narrow peak in the prefocal region. Formation of such structure is typical when two shock fronts form and collide in one period of the pressure waveform.^{30,31} The shock at a higher pressure that corresponds to the edge wave overtakes the leading shock at a lower pressure in the direct wave. When two shock fronts collide, the absorption increases sharply causing a rapid decrease of the peak positive pressure.

Spatial structure of the peak pressures and intensity in the scanning plane xz is illustrated in Fig. 10 at increasing outputs for a set of 40 active elements. The left column corresponds to the quasi linear regime (15 V) when the waveform is not greatly distorted (Fig. 8); the middle one shows distributions for stronger levels of nonlinear distortion (30 V) when the waveform contains a developed shock (Fig. 8); and the right column corresponds to the saturation regime (80 V). In all regimes, the focal regions of peak pressure and intensity are highly elongated along the z axis of the probe. With increasing applied voltage, focal regions become narrower in both the x and z directions. Note that changes in p^+ and intensity distributions with the increase in applied voltage are more pronounced than for the p^- distribution.

When nonlinear effects are present, the acoustic field structure for different numbers of operating elements differs very strongly. 2D distributions of the peak positive pressure p^+ , peak negative pressure p^- , and intensity I have fairly complicated spatial patterns (Fig. 11). In addition, the

acoustic field structure in the scanning and elevation planes (xz and yz , respectively) are very different. Dimensions of the focal areas of p^+ , p^- , and I dramatically reduce along the x axis and z axis for greater numbers of active elements but remain constant along the y axis.

Similar to the case of linear focusing (Fig. 5), the maximum values of peak pressures and intensity in the nonlinear beam are not necessarily reached at the probe axis. For example, when 16 elements are active and the beam is weakly focused, these maxima are reached off the axis in the elevation plane yz prefocally, at distances $z < 40$ mm (Fig. 11).

As in the case of linear focusing (Fig. 5), X-shaped structures are observed in the scanning plane xz of the nonlinear field of fully active array of 128 elements (Fig. 11). In the nonlinear beam, a narrow region of very high peak positive pressure in the X-shaped structure, much higher than the peak negative one, identifies locations of the shock front presence, where a strong increase in waveform asymmetry occurs. In such a field, shocks first form at the edge of the beam prefocally, and then, on the axis in the focal lobe of the beam.

Note that a very specific structure of the focal zone is observed for the set of 128 active elements (Fig. 11). In this case, the width of the focal volume of the peak positive pressure along the x axis is only $50 \mu\text{m}$, half the diameter of the FOPH tip ($100 \mu\text{m}$), while it is $4 \text{ mm} \times 4 \text{ mm}$ along the y and z axes. Such a small dimension of the focal volume for p^+ in the x -direction makes it challenging to measure and is likely the reason of the significant difference (35%) between the simulated and experimental data (Figs. 6 and 7).

IV. CONCLUSION

In this work, strong nonlinear propagation effects were analyzed in the field generated by a standard abdominal

imaging probe (Philips C5-2) using a combined measurement and modeling approach. Linear field measurements in water were used to set a boundary condition to the model. Nonlinear simulations were performed in a wide range of the operational source voltages to analyze in detail the 3D distributions of the peak positive and peak negative pressures, and the intensity of the field. FOPH measurements were used to validate the results of nonlinear modeling.

It was shown that nonlinear waveform distortion, formation of shocks, and even saturation effects were strongly pronounced for the array probe at output levels achievable with the probes and voltages available on diagnostic machines. Formation of fully developed shocks occurred in water at acoustic outputs about one third (30 V) of the highest operational level of the system (90 V) used in the feasibility test of repositioning kidney stones in humans. Saturation of the peak positive pressure was observed at 45 V when all 128 elements were excited and at the highest operational level of 90 V in the case of 16 active elements. A significant shift (up to 1 cm) of the axial locations of the maxima of the peak pressures and intensity was observed for 40 active elements. For the set of all 128 active elements, the focusing occurred in a very localized (tens of microns) region in the array scanning plane.

Accurate acoustic characterization of the diagnostic probe performed in this study showed strong nonlinear propagation and shock formation effects that occur in water at outputs relevant to therapeutic technologies currently under development. Note that recent modeling and experimental studies for nonlinear HIFU fields have shown that formation of shocks and saturation effects observed in water also occur *in situ* at a higher output of the source scaled to compensate for the attenuation losses in tissue.^{32,33} The study of the current paper for the diagnostic probe is therefore important as the first step in estimating *in situ* fields in the human body for ensuring safety of imaging and therapy applications, and may help to optimize kidney stone propulsion.

ACKNOWLEDGMENTS

Work was supported by NIH NIBIB EB007643, NIDDK P01 DK43881, Russian Science Foundation 14-12-00974, NSBRI through NASA NCC 9-58, and a stipend of the President of Russia. The authors are grateful to Barbrina Dunmire for helpful comments.

- ¹K. R. Nightingale, C. C. Church, G. Harris, K. A. Wear, M. R. Bailey, P. L. Carson, H. Jiang, K. L. Sandstrom, T. L. Szabo, and M. C. Ziskin, "Conditionally increased acoustic pressures in nonmetal diagnostic ultrasound examinations without contrast agents: A preliminary assessment," *J. Ultrasound Med.* **34**, 1–41 (2015).
- ²J. R. Doherty, G. E. Trahey, K. R. Nightingale, and M. L. Palmeri, "Acoustic radiation force elasticity imaging in diagnostic ultrasound," *IEEE Trans. Ultrason. Ferroelectr. Freq. Control* **60**(4), 685–701 (2013).
- ³J. D. Harper, B. Dunmire, Y. N. Wang, J. C. Simon, H. D. Liggitt, M. Paun, B. W. Cunitz, F. Starr, M. R. Bailey, K. Penniston, F. C. Lee, R. S. His, and M. D. Sorensen, "Preclinical safety and effectiveness studies of ultrasonic propulsion of kidney stones," *Urology* **84**(2), 484–493 (2014).
- ⁴A. Shah, N. Owen, W. Lu, B. Cunitz, P. Kaczowski, J. Harper, M. Bailey, and L. Crum, "Novel ultrasound method to reposition kidney stones," *Urol. Res.* **38**(6), 491–495 (2010).
- ⁵P. C. May, M. R. Bailey, and J. D. Harper, "Ultrasonic propulsion of kidney stones," *Curr. Opin. Urol.* **26**(3), 264–270 (2016).

- ⁶C. D. Scales, A. C. Smith, J. M. Hanley, C. S. Saigal, and Urologic Diseases in America Project, "Prevalence of kidney stones in the United States," *Eur. Urol.* **62**(1), 160–165 (2012).
- ⁷A. Skolarikosa, G. Alivizatos, and J. Rosetteb, "Extracorporeal shock wave lithotripsy 25 years later: Complications and their prevention," *Eur. Urol.* **50**(5), 981–990 (2006).
- ⁸M. M. Osman, Y. Alfano, S. Kamp, A. Haecker, P. Alken, M. S. Michel, and T. Knoll, "5-year-follow-up of patients with clinically insignificant residual fragments after extracorporeal shockwave lithotripsy," *Eur. Urol.* **47**(6), 860–864 (2005).
- ⁹M. S. Pearle, J. E. Lingeman, R. Leveillee, R. Kuo, G. M. Preminger, R. B. Nadler, J. Macaluso, M. Monga, U. Kumar, J. Dushinski, D. M. Albalá, J. S. Wolf, D. Assimos, M. Fabrizio, L. C. Munch, S. Y. Nakada, B. Auge, J. Honey, K. Ogan, J. Pattaras, E. M. McDougall, T. D. Averch, T. Turk, P. Pietrow, and S. Watkins, "Prospective, randomized trial comparing shock wave lithotripsy and ureteroscopy for lower pole caliceal calculi 1 cm or less," *J. Urol.* **173**(6), 2005–2009 (2005).
- ¹⁰O. A. Sapozhnikov and M. R. Bailey, "Radiation force of an arbitrary acoustic beam on an elastic sphere in a fluid," *J. Acoust. Soc. Am.* **133**(2), 661–676 (2013).
- ¹¹J. D. Harper, B. W. Cunitz, B. Dunmire, F. C. Lee, M. D. Sorensen, R. S. Hsi, J. Thiel, H. Wessells, J. E. Lingeman, and M. R. Bailey, "First-in-human feasibility trial of ultrasonic propulsion of kidney stones," *J. Urol.* **195**(4), 956–964 (2016).
- ¹²T. Christopher and E. L. Carstensen, "Finite amplitude distortion and its relationship to linear derating formulae for diagnostic ultrasound systems," *Ultrasound Med. Biol.* **22**(8), 1103–1116 (1996).
- ¹³O. V. Bessonova, V. A. Khokhlova, M. R. Bailey, M. S. Canney, and L. A. Crum, "Focusing of high power ultrasound beams and limiting values of shock wave parameters," *Acoust. Phys.* **55**(4–5), 463–473 (2009).
- ¹⁴M. A. Averkiou, "Tissue harmonic imaging," in *IEEE Ultrasonics Symposium* (2000), pp. 1563–1572.
- ¹⁵X. Yang and R. O. Cleveland, "Time domain simulation of nonlinear acoustic beams generated by rectangular pistons with application to harmonic imaging," *J. Acoust. Soc. Am.* **117**(1), 113–123 (2005).
- ¹⁶V. A. Khokhlova, A. E. Ponomarev, M. A. Averkiou, and L. A. Crum, "Nonlinear pulsed ultrasound beams radiated by rectangular focused diagnostic transducers," *Acoust. Phys.* **52**(4), 481–489 (2006).
- ¹⁷C. Perez, H. Chen, T. J. Matula, M. M. Karzova, and V. A. Khokhlova, "Acoustic field characterization of the Duolith: Measurements and modeling of a clinical shockwave therapy device," *J. Acoust. Soc. Am.* **134**(2), 1663–1674 (2013).
- ¹⁸M. S. Canney, M. R. Bailey, L. A. Crum, V. A. Khokhlova, and O. A. Sapozhnikov, "Acoustic characterization of high intensity focused ultrasound fields: A combined measurement and modeling approach," *J. Acoust. Soc. Am.* **124**, 2406–2420 (2008).
- ¹⁹O. Bessonova and V. Wilkens, "Membrane hydrophone measurement and numerical simulation of HIFU fields up to developed shock regimes," *IEEE Trans. Ultrason. Ferroelectr. Freq. Control* **60**(2), 290–300 (2013).
- ²⁰W. Kreider, P. V. Yuldashev, O. A. Sapozhnikov, N. Farr, A. Partanen, M. R. Bailey, and V. A. Khokhlova, "Characterization of a multi-element clinical HIFU system using acoustic holography and nonlinear modeling," *IEEE Trans. Ultrason. Ferroelectr. Freq. Control* **60**(8), 1683–1698 (2013).
- ²¹J. Staudenraus and W. Eisenmenger, "Fibre-optic probe hydrophone for ultrasonic and shock-wave measurements in water," *Ultrasonics* **31**(4), 267–273 (1993).
- ²²K. A. Wear, P. M. Gammell, S. Maruvada, Y. Liu, and G. R. Harris, "Improved measurement of acoustic output using complex deconvolution of hydrophone sensitivity," *IEEE Trans. Ultrason. Ferroelectr. Freq. Control* **61**(1), 62–75 (2014).
- ²³P. J. Westervelt, "Parametric acoustic array," *J. Acoust. Soc. Am.* **35**(4), 535–537 (1963).
- ²⁴P. V. Yuldashev and V. A. Khokhlova, "Simulation of three-dimensional nonlinear fields of ultrasound therapeutic arrays," *Acoust. Phys.* **57**(3), 334–343 (2011).
- ²⁵P. B. Rosnitskiy, P. V. Yuldashev, and V. A. Khokhlova, "Effect of the angular aperture of medical ultrasound transducers on the parameters of nonlinear ultrasound field with shocks at the focus," *Acoust. Phys.* **61**(3), 301–307 (2015).
- ²⁶H. T. O'Neil, "Theory of focusing radiators," *J. Acoust. Soc. Am.* **21**, 516–526 (1949).

- ²⁷M. M. Karzova, M. V. Averianov, O. A. Sapozhnikov, and V. A. Khokhlova, "Mechanisms for saturation of nonlinear pulsed and periodic signals in focused acoustic beams," *Acoust. Phys.* **58**(1), 81–89 (2012).
- ²⁸Y. N. Makov, V. J. Sanchez-Morcillo, F. Camarena, and V. Espinosa, "Nonlinear change of the on-axis pressure and intensity maxima positions and its relation with the linear focal shift effect," *Ultrasonics* **48**, 678–686 (2008).
- ²⁹F. Camarena, S. Adrian-Martinez, N. Jimenez, and V. Sanchez-Morcillo, "Nonlinear focal shift beyond the geometrical focus in moderately focused acoustic beams," *J. Acoust. Soc. Am.* **134**(2), Pt. 2, 1463–1472 (2013).
- ³⁰V. A. Khokhlova, R. Souchon, J. Tavakkoli, O. A. Sapozhnikov, and D. Cathignol, "Numerical modeling of finite amplitude sound beams: Shock formation in the near field of a cw plane piston source," *J. Acoust. Soc. Am.* **110**(1), 95–108 (2001).
- ³¹M. Karzova, V. Khokhlova, S. Ollivier, E. Salze, and P. Blanc-Benon, "Mach stem formation for acoustic weak shock waves: Experiment and numerical modeling," *J. Acoust. Soc. Am.* **137**(6), EL436–EL442 (2015).
- ³²O. V. Bessonova, V. A. Khokhlova, M. S. Canney, M. R. Bailey, and L. A. Crum, "A derating method for therapeutic applications of high intensity focused ultrasound," *Acoust. Phys.* **56**(3), 354–363 (2010).
- ³³T. D. Khokhlova, M. S. Canney, V. A. Khokhlova, O. A. Sapozhnikov, L. A. Crum, and M. R. Bailey, "Controlled tissue emulsification produced by high intensity focused ultrasound shock waves and millisecond boiling," *J. Acoust. Soc. Am.* **130**(5), 3498–3510 (2011).